

Structural evolution and strain generation of derived-Cu catalysts during CO₂ electroreduction

Received: 4 March 2022

Accepted: 9 August 2022

Published online: 18 August 2022

Check for updates

Qiong Lei¹, Liang Huang^{2,3}, Jun Yin^{1,4}✉, Bambar Davaasuren⁵, Youyou Yuan⁵, Xinglong Dong^{1,6}, Zhi-Peng Wu¹, Xiaoqian Wang¹, Ke Xin Yao⁷, Xu Lu^{2,3}✉ & Yu Han^{1,6}✉

Copper (Cu)-based catalysts generally exhibit high C₂₊ selectivity during the electrochemical CO₂ reduction reaction (CO₂RR). However, the origin of this selectivity and the influence of catalyst precursors on it are not fully understood. We combine *operando* X-ray diffraction and *operando* Raman spectroscopy to monitor the structural and compositional evolution of three Cu precursors during the CO₂RR. The results indicate that despite different kinetics, all three precursors are completely reduced to Cu(0) with similar grain sizes (~11 nm), and that oxidized Cu species are not involved in the CO₂RR. Furthermore, Cu(OH)₂- and Cu₂(OH)₂CO₃-derived Cu exhibit considerable tensile strain (0.43%–0.55%), whereas CuO-derived Cu does not. Theoretical calculations suggest that the tensile strain in Cu lattice is conducive to promoting CO₂RR, which is consistent with experimental observations. The high CO₂RR performance of some derived Cu catalysts is attributed to the combined effect of the small grain size and lattice strain, both originating from the in situ electroreduction of precursors. These findings establish correlations between Cu precursors, lattice strains, and catalytic behaviors, demonstrating the unique ability of *operando* characterization in studying electrochemical processes.

Electrocatalytic CO₂ reduction reaction (CO₂RR) provides a versatile means of storing energy in chemical bonds while closing the anthropogenic carbon cycle¹. Although significant progress has been made in the generation of single-carbon (C₁) products (e.g., carbon monoxide, formate, methane, and methanol), in which a product selectivity of above 80% and an industrial-level current density have been achieved^{2–5}, the production of valuable multicarbon (C₂₊) products (e.g., ethylene, ethanol, and n-propanol) using CO₂RR has remained a challenge⁶.

To date, Cu-based catalysts are the main force for the production of C₂₊ products, owing to the *CO adsorption energy on Cu that favors the C–C coupling. Derived Cu catalysts, formed from the in situ reactions of oxides, hydroxides, or other oxidized Cu precursors under the reducing potentials of CO₂RR, have attracted significant attention because they typically exhibit high selectivities toward C₂₊ products^{7–9}. Although the Pourbaix diagram of Cu indicates that oxidized Cu precursors should be readily reduced to Cu(0) at negative potentials¹⁰,

¹Advanced Membranes and Porous Materials Center, Physical Sciences and Engineering Division, King Abdullah University of Science and Technology (KAUST), Thuwal 23955-6900, Saudi Arabia. ²Clean Combustion Research Center, KAUST, Thuwal 23955-6900, Saudi Arabia. ³KAUST Solar Center, KAUST, Thuwal 23955-6900, Saudi Arabia. ⁴Department of Applied Physics, The Hong Kong Polytechnic University, Hung Hom, Kowloon, 999077 Hong Kong, PR China. ⁵Imaging and Characterization Core Lab, KAUST, Thuwal 23955-6900, Saudi Arabia. ⁶KAUST Catalysis Center, KAUST, Thuwal 23955-6900, Saudi Arabia. ⁷Multi-scale Porous Materials Center, Institute of Advanced Interdisciplinary Studies, & School of Chemistry and Chemical Engineering, Chongqing University, Chongqing 400044, PR China. ✉e-mail: jun.yin@polyu.edu.hk; xu.lu@kaust.edu.sa; yu.han@kaust.edu.sa

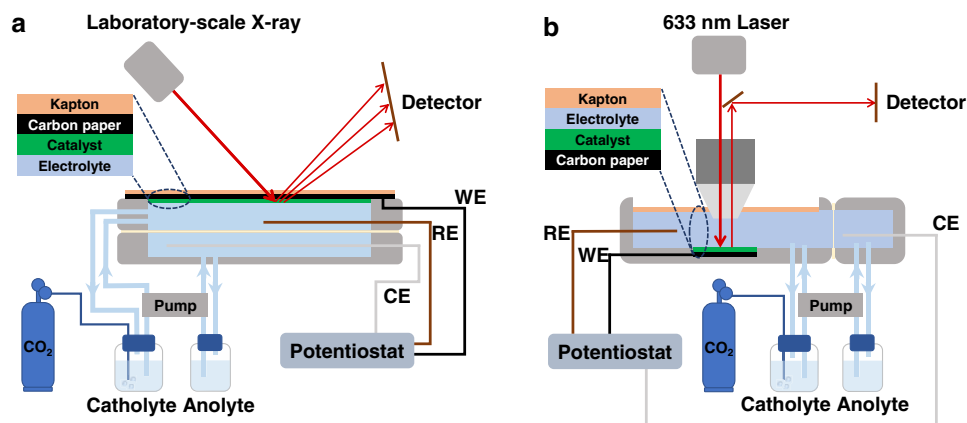


Fig. 1 | Schematic illustration of the *operando* characterization platforms. a X-ray diffraction (XRD) and **b** Raman spectroscopy for CO₂ reduction reactions (CO₂RRs) with the three investigated oxidized Cu precursors.

some experimental and theoretical studies have stated that Cu⁺ species or mixed oxidation states of Cu (e.g., Cu²⁺, Cu⁺, and Cu) are present in oxide- or hydroxide-derived Cu electrodes and are responsible for their high C₂₊ selectivity^{8,11–16}. For example, Nilsson et al. combined spectroscopy and microscopy techniques to unravel the presence of residual oxygen in oxide-derived Cu electrocatalysts under CO₂RR conditions^{17–19}. In contrast, many other studies have demonstrated the full reduction of oxidized Cu precursors to Cu(0) and attributed the enhanced C₂₊ selectivity to structural and morphological effects^{20,21}, specific crystal facet exposure^{7,22}, or grain boundary and low-coordinated sites^{23,24}. These inconsistent conclusions indicate that identifying the active species of derived Cu catalysts and the origin of their high C₂₊ selectivity remains controversial.

Lattice strain can modulate the activity and selectivity of electrocatalysts by breaking the linear scaling relationship²⁵. Using density functional theory (DFT), Mavrikakis et al. first correlated metal lattice strain, *d*-band center shift, and adsorption energy to explain catalytic behaviors²⁶. Various approaches have been employed to induce strain in Cu catalysts, including the formation of bimetallic nanoparticles^{27,28}, epitaxial growth of thin films^{29,30}, and crystal morphology engineering³¹. However, few studies have investigated strain effects in derived Cu catalysts for CO₂RR. Li et al. observed microstrains in oxide-derived Cu, but they did not correlate them with CO₂RR activity or selectivity³². Moreover, the influence of precursor materials on the catalytic performance of derived Cu catalysts has not been investigated. A better understanding of these aspects would facilitate the rational design of catalysts to achieve higher C₂₊ product selectivity.

Owing to the high sensitivity of Cu species to O₂ and their immediate re-oxidation when the reducing potential is lifted³³, *operando* characterizations are essential for probing the active species and dynamic evolution of Cu-based catalysts during CO₂RR³⁴. Particularly, some *operando* techniques, such as Raman spectroscopy, can detect the intermediates and products of CO₂RR in real time, which has significantly facilitated the investigation of the reaction mechanism and catalyst optimization^{35,36}. However, using *operando* characterization techniques that are relying on high energy beamlines (e.g., X-ray diffraction (XRD) and X-ray absorption spectroscopy) has been restricted by the limited access to synchrotron radiation facilities. The feasibility of using in-house laboratory XRD for an *operando* investigation of CO₂RR has not been fully explored.

In this study, we investigate the structural and compositional evolution of three Cu-based catalysts derived from Cu₂(OH)₂CO₃, Cu(OH)₂ and CuO during CO₂RR with an *operando* XRD platform that uses a laboratory-scale X-ray to analyze the phase transformation of the catalyst crystals (Fig. 1a) and *operando* Raman spectroscopy to detect the surface species (Fig. 1b). It is revealed that the three oxidized

Cu precursors are all completely reduced to Cu(0) when delivering their maximum Faradaic efficiencies (FE) for C₂₊ products (FE_{C₂₊}), whereas CuO shows faster electroreduction kinetics than Cu₂(OH)₂CO₃ and Cu(OH)₂. The three derived Cu catalysts exhibit significantly higher FE_{C₂₊} compared to bulk Cu, which is attributed to their small grain sizes (~11 nm). *Operando* XRD discovers that Cu(OH)₂- and Cu₂(OH)₂CO₃-derived Cu exhibit obvious tensile strains, while CuO-derived Cu is almost strain-free. This finding offers a method to induce lattice strain in Cu nanocrystals by using the appropriate precursor and explains the difference in CO₂RR activity relative to hydrogen evolution among the three derived Cu catalysts. Therefore, lattice strain has been identified as another factor promoting the CO₂RR activity of derived Cu catalysts in addition to grain boundaries and high-index facets associated with the small grain size. These important insights cannot be gained by ex situ characterization because Cu nanocrystals undergo rapid surface oxidation and strain relaxation once electroreduction conditions are lifted. This study highlights the importance and necessity of *operando* characterizations in probing the evolution of electrocatalysts, and provides a technical solution for achieving this goal in ordinary laboratories.

Results

Precursor characterization

The XRD characterization revealed that the three synthesized precursors, Cu₂(OH)₂CO₃, Cu(OH)₂, and CuO, are all phase pure (Supplementary Fig. 1a), and their Raman spectra were perfectly matched with the reported standard spectra (Supplementary Fig. 2a, b)^{36–39}. Scanning electron microscopy (SEM) revealed that Cu₂(OH)₂CO₃ consisted of agglomerated nano-sized square rods (Supplementary Fig. 3a), whereas Cu(OH)₂ exhibited a flower-like morphology, formed by the radial stacking of rectangular nanosheet bundles (Supplementary Fig. 3b). As the CuO sample was synthesized by heating the as-prepared Cu₂(OH)₂CO₃, it retained the morphology of the parent material (Supplementary Fig. 3c) but had smaller grains, which could be attributed to the 60% atomic loss during conversion. The mean crystallite (grain) sizes of the Cu₂(OH)₂CO₃, Cu(OH)₂, and CuO nanocrystals estimated from the XRD data using the Scherrer equation were 24.7 ± 3.5, 19 ± 0.5, and 10 ± 0.5 nm, respectively (Supplementary Table 1).

CO₂RR performance

We evaluated the CO₂RR performance of the three Cu based catalysts with an H-type cell by analyzing the gas and liquid products at different applied potentials in CO₂-saturated 0.1 M KHCO₃ aqueous solution in ambient conditions. The maximum FE_{C₂₊} of Cu₂(OH)₂CO₃, Cu(OH)₂, and CuO-derived Cu catalysts were 73.0, 71.9, and 68.6% at -1.05,

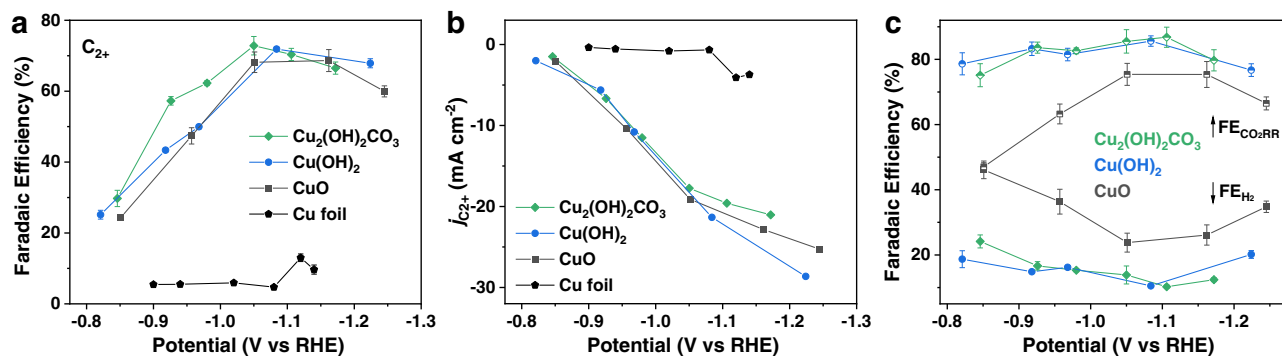


Fig. 2 | Electrochemical CO₂RR performances. Comparison of **a** Faradaic efficiency of C₂₊ products and **b** C₂₊ partial current density for Cu₂(OH)₂CO₃, Cu(OH)₂, and CuO nanocrystals and Cu foil. Data are normalized using the geometric surface area. **c** Comparison of Faradaic efficiencies for overall CO₂RR (FE_{CO₂RR}) and HER

(FE_{H₂}) between Cu₂(OH)₂CO₃, Cu(OH)₂, and CuO nanocrystals. All CO₂RR experiments were performed in an H-type cell using CO₂-saturated 0.1 M KHCO₃ as the electrolyte for 1.5 h. Error bars represent the standard deviation of three independent measurements.

-1.08, and -1.16 V_{RHE}, respectively, substantially higher than the FE_{C₂₊} obtained on electropolished Cu foil (13% at -1.12 V_{RHE}; Fig. 2a). The main C₂₊ products of the systems included C₂H₄, C₂H₅OH, n-C₃H₇OH, C₂H₅CHO, CH₃CHO, and C₂H₆ (sequenced by decreasing FE, see Supplementary Fig. 4a–c for the detailed product distribution). The three catalysts exhibited similar C₂₊ partial current densities (j_{C₂₊}) within the tested potential window, reaching -20 to -30 mA cm⁻² at -1.2 V_{RHE}. In contrast, the maximum j_{C₂₊} value obtained on the Cu foil was -4.1 mA cm⁻² at -1.12 V_{RHE} (Fig. 2b). The observed high C₂₊ selectivities and activities of Cu(OH)₂- and CuO-derived Cu are consistent with findings in previous studies^{7,8,40}, whereas this is the first report on the high selectivity and activity of Cu₂(OH)₂CO₃-derived Cu toward C₂₊ production during CO₂RR.

The overall FEs for CO₂RR (FE_{CO₂RR}) of the three catalysts followed the order of Cu₂(OH)₂CO₃ ≈ Cu(OH)₂ > CuO (Fig. 2c). Specifically, Cu₂(OH)₂CO₃- and Cu(OH)₂-derived Cu exhibited ~75% FE_{CO₂RR} at a relatively low potential of -0.83 V_{RHE}, whereas the FE_{CO₂RR} of CuO was only ~47% at this potential. Correspondingly, the competing hydrogen evolution reaction (HER) occurred to a significantly higher degree on CuO-derived Cu than on the other two catalysts over the tested potential range. The three catalysts exhibited a similar trend: as the potential became more negative, the FE for hydrogen (FE_{H₂}) first decreased and then increased. The minimum FE_{H₂} (i.e., the maximum FE_{CO₂RR}) was reached at -1.1 V_{RHE}, where the difference in CO₂RR activity (or HER activity) between CuO and the other two catalysts became less significant but still discernible (Fig. 2c).

Redox behaviors. To further examine the catalyst evolution during CO₂RR, we first investigated the redox behaviors of the three oxidized Cu precursors by performing Cyclic Voltammetry (CV) in 0.1 M KOH aqueous solution and Linear Sweep Voltammetry (LSV) in Ar-saturated 0.1 M of KHCO₃ aqueous solution. The results revealed that, in both KOH and KHCO₃ environments, the three samples undergo the same electroreduction pathway (i.e., complete reduction to Cu via the formation of Cu₂O); however, more negative potentials are required for the electroreduction of Cu₂(OH)₂CO₃ and Cu(OH)₂ compared to CuO (see Supplementary Note and Supplementary Fig. 5 for the detailed analysis).

Operando XRD. We then performed time-resolved *operando* XRD in a customized flow cell to investigate the structural transitions of the three oxidized Cu precursors during CO₂RR (Supplementary Figs. 6 and 7). When Cu₂(OH)₂CO₃ was at its optimal C₂₊ production potential (-1.05 V_{RHE}), its characteristic (20-1) peak at 31.3° gradually faded during the first 45 min of the reaction, while the fingerprint (111) and (200) peaks of metallic Cu emerged with increasing

intensity after the first 15 min (Fig. 3a). No diffraction peaks related to Cu hydroxides or oxides were detected during the entire process, suggesting that these species, if present, did not form crystalline phases. Further analysis of *operando* XRD data collected at different potentials revealed the potential-dependent electroreduction kinetics of Cu₂(OH)₂CO₃: the required reduction time from Cu₂(OH)₂CO₃ to Cu decreased with an increase in the negativity of the applied potential (Supplementary Fig. 8a, b). Similar to Cu₂(OH)₂CO₃, Cu(OH)₂ underwent a relatively slow process before the complete reduction to metallic Cu, during which no crystalline CuO or Cu₂O phase was detected. At its optimal potential for FE_{C₂₊} (-1.08 V_{RHE}), the strongest (130) peak at 39.8° vanished completely after 60 min of CO₂RR, even though metallic Cu emerged in the first 15 min (Fig. 3b). In contrast, CuO was rapidly and completely converted to metallic Cu within the first 15 min of CO₂RR (Fig. 3c), implying faster electroreduction kinetics compared to Cu₂(OH)₂CO₃ and Cu(OH)₂. On the other hand, although the grain sizes of the starting materials were different (Supplementary Table 1), the Cu derived from the three precursors had similar grain sizes (~11 nm; estimated from the XRD data; Supplementary Table 1). The smaller mean grain sizes of the derived Cu relative to those of the parent materials could be attributed to the combined effect of the volume shrinkage of the unit-cell and crystal fragmentation⁷. We therefore concluded that the three oxidized Cu precursors, despite the differences in their chemical components and electroreduction kinetics, were completely reduced to metallic Cu with similarly small grain sizes while (or before) delivering enhanced C₂₊ selectivity under the CO₂RR conditions.

Interestingly, Cu nanocrystals derived from Cu₂(OH)₂CO₃ exhibited shifted XRD peaks relative to the Cu foil as a standard sample, implying the presence of lattice strain. Specifically, at -1.05 V_{RHE}, the Cu(111) and Cu(200) diffraction peaks were shifted by -0.25° and -0.39° to the low-angle direction (Fig. 3d), corresponding to the tensile strains of 0.55% and 0.72%, respectively (Supplementary Table 2). This phenomenon was reproduced in measurements at different potentials, whereas the degree of strain slightly varied with the potential (Supplementary Table 2). Similarly, Cu nanocrystals derived from Cu(OH)₂ possessed significant (0.42%–0.47%) tensile strains under CO₂RR conditions, according to the shift in the Cu(111) diffraction peak (Fig. 3d and Supplementary Table 2). In contrast, Cu derived from CuO displayed negligible peak shifts relative to the standard regardless of the applied potential, although it had a grain size similar to the other two derived Cu samples (Fig. 3d and Supplementary Table 2). The *operando* XRD data were all corrected based on the results of a standard sample to eliminate liquid-induced peak shift effects (Supplementary Fig. 9).

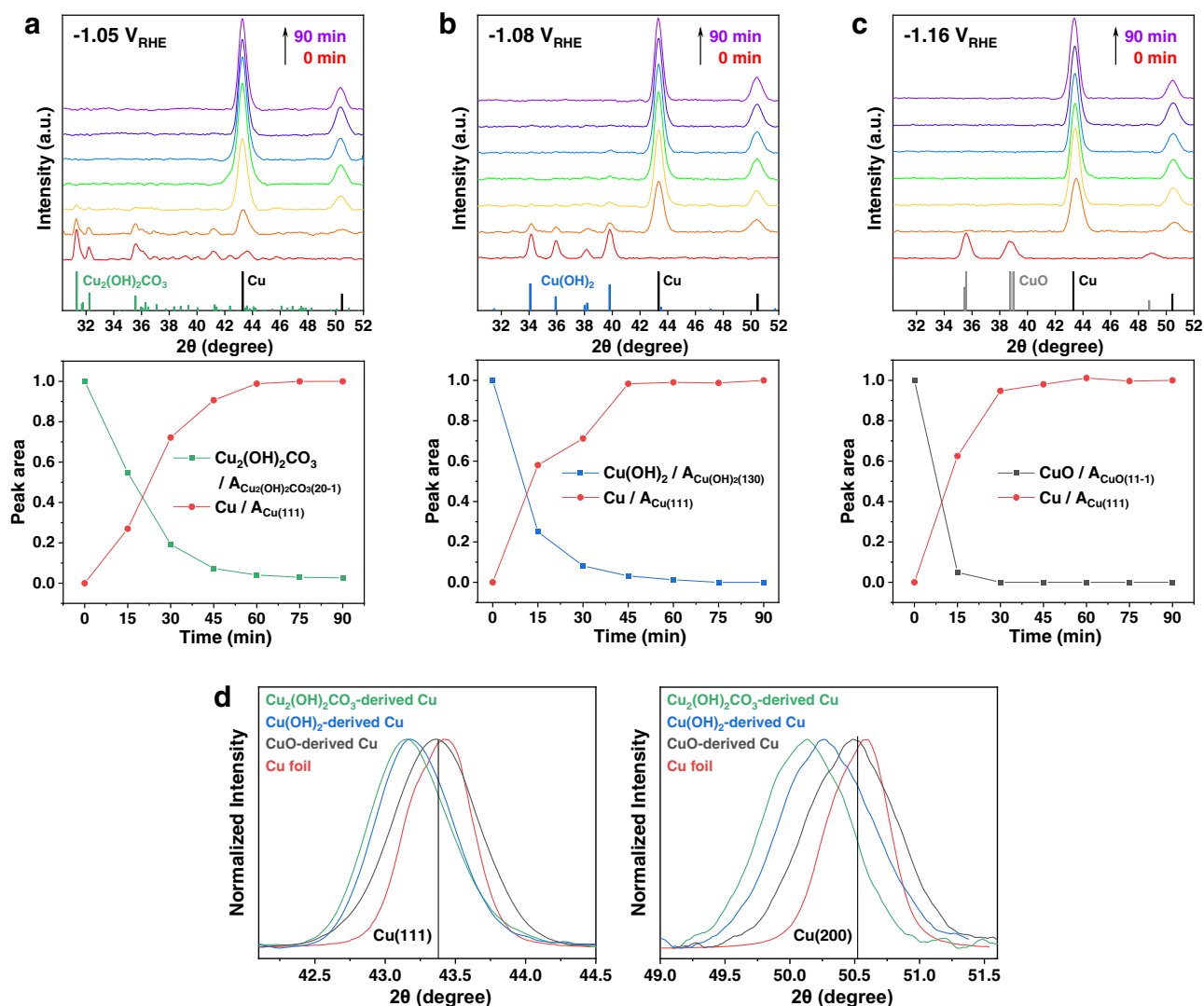


Fig. 3 | The *operando* X-ray diffraction (XRD) characterizations. Time-resolved *operando* XRD patterns (upper panel) and the corresponding quantitative peak analysis (lower panel) of **a** $Cu_2(OH)_2CO_3$, **b** $Cu(OH)_2$, and **c** CuO nanocrystals during the CO_2RR at their optimum potential for C_{2+} production. Spectra were collected every 15 min. For the quantitative peak analysis, the integrated and

normalized intensities of $Cu_2(OH)_2CO_3(20-1)$, $Cu(OH)_2(130)$, $CuO(11-1)$ and $Cu(111)$ were used. **d** Comparison of Cu(111) (left panel) and Cu(200) (right panel) diffraction peak position of various derived Cu and Cu foil measured from *operando* XRD experiments. Vertical lines indicate the standard diffraction peak positions.

Operando Raman spectroscopy. Time-resolved *operando* Raman spectroscopy was performed in a customized flow cell to explore the oxidation state evolution of the catalyst surface during CO_2RR (Supplementary Figs. 10 and 11). When the measurement of $Cu_2(OH)_2CO_3$ was conducted at $-0.84 V_{RHE}$, some areas of the electrode surface gradually changed from the initial turquoise color (the color of $Cu_2(OH)_2CO_3$ nanocrystals) to brown after 90 min of CO_2RR (Fig. 4a, right panel). Three types of Raman spectra were observed in different regions of the electrode surface, including the characteristic spectrum of $Cu_2(OH)_2CO_3$ from the remaining shiny crystals and two distinct spectra from the newly formed brown area (Fig. 4a, left panel). Further analysis revealed that the red-circled region corresponded to Cu_2O , as evidenced by the fingerprint Raman bands at 149, 528, and 620 cm^{-1} ^{136,41}. The spectrum acquired from the blue-circled region revealed three intense bands at 283, 368, and 530 cm^{-1} and a shoulder band at 498 cm^{-1} . According to recent studies, the bands at 283 and 368 cm^{-1} correspond to the frustrated rotational mode of $*CO$ (P1) and the $Cu(0)-CO$ stretching vibration (P2), respectively^{35,41}, and the bands at 498 and 530 cm^{-1} originate from C-containing adsorbates⁴²⁻⁴⁴. Interestingly, once the negative

potential of CO_2RR was lifted, these four bands disappeared, whereas the fingerprint pattern of Cu_2O emerged (Supplementary Fig. 12a), confirming their association with the binding intermediates to the Cu surface. These results taken together indicate that the catalyst in the blue-circled region was fully reduced to Cu(0), and the Raman bands at 283, 368, 498 (shoulder), and 530 cm^{-1} can be regarded as indicators for the formation of Cu(0) and its participation in the CO_2RR process.

Given that the shiny crystals were confirmed to be unreduced $Cu_2(OH)_2CO_3$, subsequent analyses were performed on the brown region of the electrode. At a more negative potential (e.g., $-1.05 V_{RHE}$ in Fig. 4b, and $-1.2 V_{RHE}$ in Supplementary Fig. 13), the color change of the electrode surface was faster, and few shiny crystals remained on the electrode after 30 min. Moreover, most acquired Raman spectra exhibited a similar pattern (283, 368, 498 (shoulder), and 530 cm^{-1}), suggesting the predominance of Cu(0) during CO_2RR at such negative potentials. Slight deviations within 280 to 284 and 368 to 388 cm^{-1} for the $Cu(0)-CO$ signals can be attributed to the dynamic change in the Cu surface during CO_2RR ⁴⁵. The other two characteristic Raman bands also shifted within 486 to 500 and 526

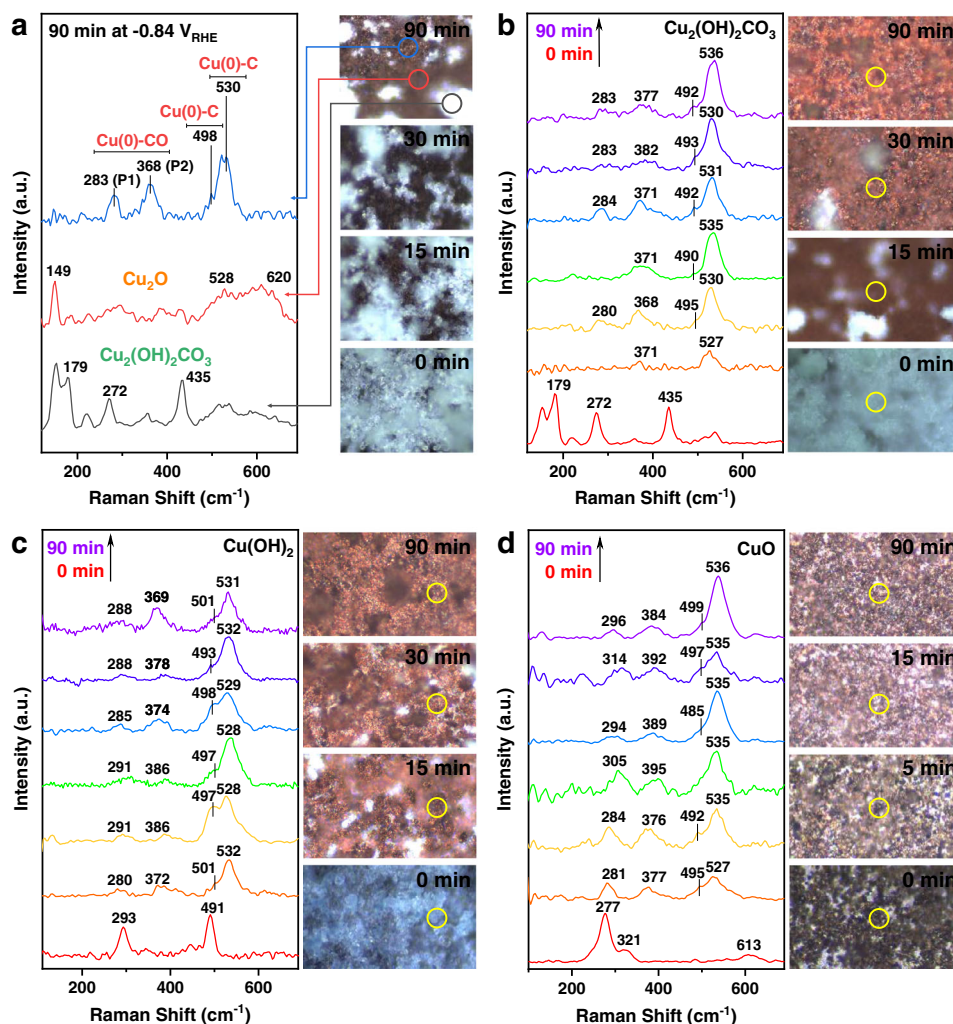


Fig. 4 | The *operando* Raman spectroscopy characterizations. **a** Time-resolved light microscopy (right panel) images of the $\text{Cu}_2(\text{OH})_2\text{CO}_3$ electrode surface during the CO_2RR process at $-0.84 \text{ V}_{\text{RHE}}$, and the *operando* Raman spectra (left panel) acquired from three different areas (circled in different colors) on the $\text{Cu}_2(\text{OH})_2\text{CO}_3$ electrode surface after 90 min of the reaction. Time-resolved *operando* Raman

spectra (left panel) and light microscopy (right panel) images of the **b** $\text{Cu}_2(\text{OH})_2\text{CO}_3$, **(c)** $\text{Cu}(\text{OH})_2$, and **d** CuO nanocrystals at their optimum potential for C_2^+ production during CO_2RR . The circles indicate the locations of the laser spot with a theoretical diameter of 858 nm. Spectra were collected every 15 min.

to 536 cm^{-1} , presumably due to the variation in the C-containing species binding to the Cu surface.

Operando Raman measurements indicated that, similar to $\text{Cu}_2(\text{OH})_2\text{CO}_3$, $\text{Cu}(\text{OH})_2$ also underwent gradual and uneven electroreduction under CO_2RR conditions (Fig. 4c). In contrast, CuO exhibited a much faster electroreduction rate. The original black electrode surface turned completely brown within the first 5 min. The Raman bands of CuO vanished within 15 min, while $\text{Cu}(\text{O})$ dominated the electrode surface (Fig. 4d). These observations are consistent with the bulk behaviors of the three precursors revealed through *operando* XRD.

In summary, the *operando* Raman spectroscopy echoes and complements the *operando* XRD analysis. Both methods demonstrate that the three oxidized Cu precursors (bulk and surface) are fully reduced to metallic Cu when delivering their maximum $\text{FE}_{\text{C}_2^+}$, and that CuO exhibits faster reduction kinetics than the other two. Another interesting finding is that Raman signals associated with the CO_2RR intermediates and signals of $\text{Cu}_2(\text{OH})_2\text{CO}_3$, $\text{Cu}(\text{OH})_2$, CuO , or Cu_2O do not appear in the same region simultaneously. Given that XRD can only detect crystalline phases and Raman effect is weak and localized, the present data cannot completely rule out the possible presence of metastable, short-lived, amorphous oxidized Cu species in the derived Cu catalysts^{16,46}.

Discussion

Importance and necessity of *Operando* characterizations

Operando characterizations provide otherwise unavailable information on the inherent states of catalysts and intermediates under reaction conditions and are particularly important for systems involving susceptible species, such as Cu. In this study, the Raman bands, which are relevant to the binding of CO_2RR intermediates to $\text{Cu}(\text{O})$ (i.e., 283, 368, 498 (shoulder), and 530 cm^{-1}), could not be observed through ex situ measurements due to the inevitable rapid surface oxidation of Cu (Supplementary Fig. 12a). In other words, without *operando* Raman spectroscopy, we would not have been able to determine the lack of co-occurrence of CO_2RR intermediates and oxidized Cu species, which is crucial for determining the catalytic active species (*ubi infra*).

Likewise, significant tensile strains in $\text{Cu}_2(\text{OH})_2\text{CO}_3$ and $\text{Cu}(\text{OH})_2$ -derived Cu could only be probed using *operando* XRD. When the electrodes containing derived Cu nanocrystals were removed from the electrochemical systems and characterized using conventional (ex situ) XRD, the $\text{Cu}(111)$ and $\text{Cu}(200)$ diffraction peaks appeared at their standard positions without a shift (Supplementary Fig. 12b). Moreover, a broad peak emerged at -36.62° , which could be assigned to Cu_2O formed through surface oxidation. We surmise that the surface oxidation of Cu nanocrystals leads to the relaxation of the lattice

strain. These results demonstrate the unique ability of *operando* characterization to capture the true states of catalysts under reaction conditions.

In addition, the time-resolved *operando* characterizations revealed that the electroreduction kinetics of CuO are faster than those of $\text{Cu}_2(\text{OH})_2\text{CO}_3$ and $\text{Cu}(\text{OH})_2$. We note that the electroreduction behaviors of $\text{Cu}_2(\text{OH})_2\text{CO}_3$ and $\text{Cu}(\text{OH})_2$ under the CO_2RR conditions have not been previously investigated using *operando* techniques, while the conclusions of several earlier studies on Cu oxides^{41,47} are consistent with the observations of the CuO sample in this work.

Determination of active species in derived Cu catalysts

The *operando* XRD and *operando* Raman spectroscopy results collectively suggest that, despite the difference in chemical components and electroreduction kinetics, the three oxidized Cu precursors were reduced to metallic Cu while (or before) delivering enhanced C_{2+} selectivity under CO_2RR conditions. For $\text{Cu}_2(\text{OH})_2\text{CO}_3$ and $\text{Cu}(\text{OH})_2$ with slow electroreduction kinetics, the temporary presence of mixed Cu oxidation states (Cu^{2+} from $\text{Cu}_2(\text{OH})_2\text{CO}_3$ or $\text{Cu}(\text{OH})_2$, Cu^+ from Cu_2O , and metallic Cu) was observed; however, Raman signals related to CO_2RR intermediates (283, 368, 498 (shoulder), and 530 cm^{-1}) were only observed in regions without Raman fingerprints of $\text{Cu}_2(\text{OH})_2\text{CO}_3$, $\text{Cu}(\text{OH})_2$, CuO, or Cu_2O . These results rule out the participation of these oxidized Cu species in CO_2RR ; thus, we conclude that Cu(0) is the catalytic active site responsible for enhanced C_{2+} selectivity.

Based on this understanding, we speculate that, at the initial stage of the reaction, CuO is more selective for C_{2+} products than $\text{Cu}_2(\text{OH})_2\text{CO}_3$ because CuO can be reduced to Cu(0) in a shorter time. To verify this speculation, we re-examined the $\text{Cu}_2(\text{OH})_2\text{CO}_3$ and CuO systems by monitoring the C_{2+} production rate during the CO_2RR at optimal potentials. Because C_2H_4 was the main component among the C_{2+} products in these systems, we used $\text{FE}_{\text{C}_2\text{H}_4}$ as the indicator for C_{2+} selectivity. The results revealed that the $\text{FE}_{\text{C}_2\text{H}_4}$ plateau was achieved faster in the CuO system than in the $\text{Cu}_2(\text{OH})_2\text{CO}_3$ system, although the final $\text{FE}_{\text{C}_2\text{H}_4}$ values of the two systems were similar. At sampling points of 10, 15, and 20 min, CuO exhibited a higher $\text{FE}_{\text{C}_2\text{H}_4}$ than $\text{Cu}_2(\text{OH})_2\text{CO}_3$ (Supplementary Fig. 14). This result agrees with the expectation, confirming that Cu(0) plays a key role in enhancing C_{2+} selectivity.

If Cu(0) is indeed the origin of high C_{2+} selectivity and oxidized Cu precursors are reduced to metallic Cu during CO_2RR , the marked variation in the performance of various Cu catalysts reported in the literature need to be understood. For instance, why do hydroxide- or oxide-derived Cu catalysts generally exhibit higher C_{2+} selectivity than bulk Cu catalysts (e.g., Cu foil)? In a previous study, we demonstrated that an oxidation–reduction cycle resulted in the fragmentation of original Cu material into smaller irregular grains⁷, leading to the exposure of a variety of grain boundaries and high-index facets promoting C–C couplings for high $\text{FE}_{\text{C}_{2+}}$ ^{32,48–53}. We therefore postulate that the C_{2+} selectivity is roughly related to the mean grain (crystallite) size of the Cu catalyst, and is benefited from grains that are more irregular with a decreased size.

In this study, the three derived Cu catalysts with similar grain sizes (~11 nm) indeed exhibited similar $\text{FE}_{\text{C}_{2+}}$ (68%–73%). To further verify the correlation between the Cu grain size and C_{2+} selectivity, two additional Cu samples were prepared: Cu nanowires and electropolished polycrystalline Cu foil (Supplementary Figs. 1b and 3d–f). The mean grain size of the Cu nanowires estimated by XRD was ~29 nm, and the transmission electron microscopy revealed that the Cu foil comprised micron-sized grains (Supplementary Fig. 3e). The CO_2RR performance of Cu nanowires and electropolished polycrystalline Cu foil was also evaluated (Supplementary Fig. 4d–e). Comparisons of the maximum $\text{FE}_{\text{C}_{2+}}$ and the mean grain sizes of the five tested catalysts confirmed a negative correlation between these two factors; that is, the C_{2+} selectivity increased with a decreasing Cu grain size (Fig. 5a). Another consequence of reducing the Cu grain size is an increase in the

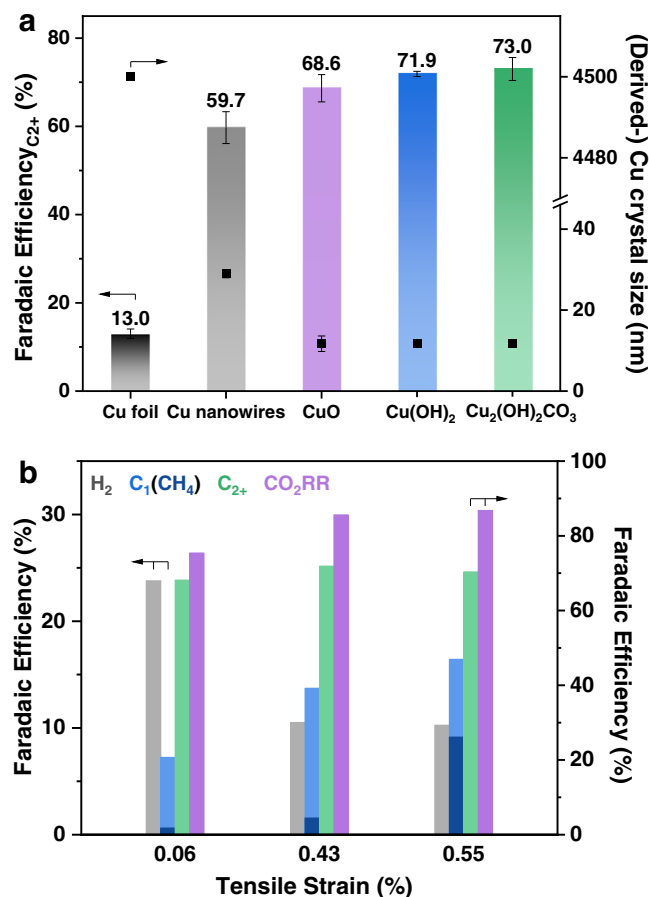


Fig. 5 | Size and strain effects on CO_2RR behaviors of Cu-based catalysts.

a Maximum Faradaic efficiencies for C_{2+} products and the crystal sizes of the derived Cu (from $\text{Cu}_2(\text{OH})_2\text{CO}_3$, $\text{Cu}(\text{OH})_2$, and CuO nanocrystals), Cu nanowires, and polycrystalline Cu foil. **b** Different tensile strain values of the derived Cu (along the [111] direction) and the corresponding Faradaic efficiencies for H_2 , C_1 , CH_4 , C_{2+} products, and the overall CO_2RR at $-1.1\text{ V}_{\text{RHE}}$. Samples with 0.06%, 0.43%, and 0.55% tensile strains represent the Cu derived from CuO, $\text{Cu}(\text{OH})_2$, and $\text{Cu}_2(\text{OH})_2\text{CO}_3$, respectively. Error bars represent the standard deviation of three independent measurements.

electrochemically active surface area of the electrode (Supplementary Table 1), which typically results in enhanced apparent activity in terms of current density per unit electrode area⁵⁴.

Strain effects

Although the three derived Cu catalysts exhibited similar C_{2+} selectivity, a discernible difference exists in the overall Faradaic efficiency for CO_2RR ($\text{FE}_{\text{CO}_2\text{RR}}$) between CuO and the other two catalysts ($\text{CuO} < \text{Cu}_2(\text{OH})_2\text{CO}_3 \approx \text{Cu}(\text{OH})_2$; Fig. 2c). Moreover, CuO-derived Cu is strain-free, whereas the other two derived Cu samples show significant tensile strains under the CO_2RR conditions (Fig. 3d). This coincidence led to wondering whether lattice strain is another factor affecting the catalytic performance of Cu in addition to grain boundaries and high-index facets associated with the small grain size.

According to the *d*-band theory, lattice strain can trigger a shift of the *d*-band center of the metal and tailor its catalytic activity^{25,26,29,30}. We performed DFT calculations to investigate how tensile strain affects the *d*-band center of Cu and the consequent binding energy (E_{binding}) of *CO on its surface, using Cu(111) and Cu(100) with different strain values as model structures (see the computational details in the Methods). The calculations revealed that for both structures, the *d*-band center shifts up toward the Fermi Level with increasing tensile

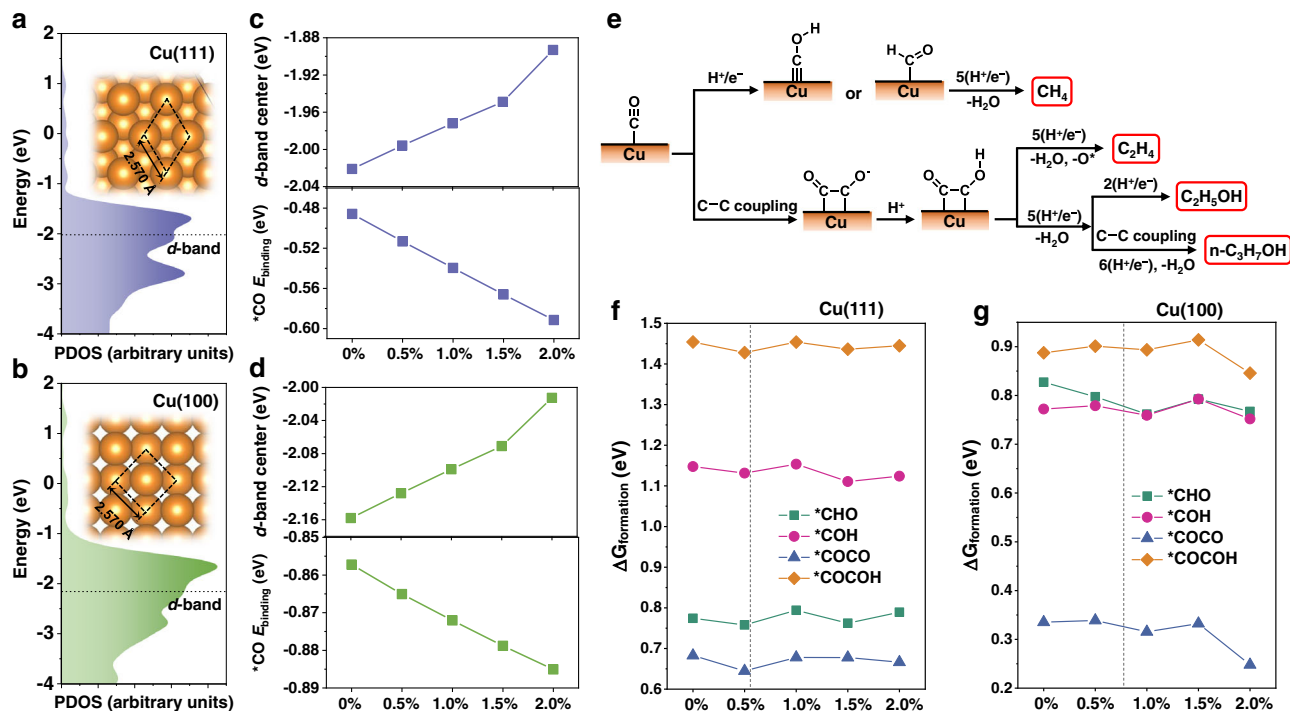


Fig. 6 | The DFT calculation results. Projected density of states (PDOS) of the d -band for **a** Cu(111) and **b** Cu(100) without strain. The horizontal black dashed lines indicate positions of the d -band center (referenced to the Fermi level). The Fermi level was set as zero. Insets are top views of the corresponding crystal structure slabs. Calculated d -band centers and binding energies of *CO for **c** Cu(111) and **d** Cu(100) with different strain values (0.0%, 0.5%, 1.0%, 1.5% and 2.0%). For Cu(111), the *CO coverage is 0.25 monolayer (ML) with a cross-sectional area of

$9.15 \times 10^{-15} \text{ cm}^2$; for Cu(100), the *CO coverage is 0.11 ML with a cross-sectional area of $1.20 \times 10^{-14} \text{ cm}^2$. **e** Reaction pathway for the formation of CH_4 and typical C_{2+} products during CO_2RR . The calculated Gibbs free energies of formation ($\Delta G_{\text{formation}}$) of *CHO, *COH, *COCO, and *COCOH on **f** Cu(111) and **g** Cu(100) with different strain values. The vertical grey dashed lines indicate the experimental tensile strain of 0.55% for Cu(111) and 0.72% for Cu(100). All the DFT calculations were performed at the GGA/PBE level of theory.

strain, thus leading to a continuous increase in the E_{binding} of *CO. This conclusion holds for both low (Fig. 6a–d) and high (Supplementary Fig. 15a–c) *CO surface coverages. These results imply that strained Cu has a greater promoting effect on *CO adsorption than unstrained Cu, which has been experimentally verified using a recently reported method based on Raman band analysis (Supplementary Fig. 16a–d)⁵⁵.

According to the widely accepted CO_2RR mechanism^{56–59}, *CHO/*COH and *COCO/*COCOH are the primary intermediates for the formation of CH_4 and C_{2+} products, respectively (Fig. 6e), while the Gibbs free energies of formation ($\Delta G_{\text{formation}}$) of these intermediates are indicators of the ease of the corresponding pathways. The introduction of 0.5% tensile strain slightly reduces the $\Delta G_{\text{formation}}$ of *CHO, *COH, *COCO, and *COCOH on Cu(111) by 0.02, 0.02, 0.04, and 0.03 eV, respectively; further increases in strain do not monotonically decrease their $\Delta G_{\text{formation}}$ on Cu(111) but lead to fluctuations (Fig. 6f and Supplementary Fig. 17). Introducing 0.5–1.0% tensile strain leads to a decrease in $\Delta G_{\text{formation}}$ for *CHO, *COH, and *COCO on Cu(100), and further increasing the strain causes their $\Delta G_{\text{formation}}$ to first increase and then decrease. For *COCOH on Cu(100), the $\Delta G_{\text{formation}}$ slightly increases when the tensile strain increases from 0.0% to 1.5%, followed by a sudden drop at 2.0% strain (Fig. 6g and Supplementary Fig. 17).

Moreover, we explored the strain effect on the HER by calculating the adsorption free energy of *H (ΔG_{H}) and water dissociation activation barriers. Regardless of strain degree and surface type, the ΔG_{H} is uphill whereas the H_2 removal is downhill, implying that the HER on Cu is limited by the *H formation (Supplementary Fig. 18a, b). For Cu(111), although the ΔG_{H} decreases with increasing tensile strain, it remains considerably positive at large strain values (e.g., 0.07 eV at 2.0% strain). For Cu(100), tensile strain does not affect the ΔG_{H} . The influence of tensile strain on the water dissociation activation barrier is marginal for both surfaces (Supplementary Fig. 18c, d).

In summary, the calculations indicate that the introduction of tensile strain in Cu significantly promotes the adsorption of *CO and also slightly facilitates the subsequent hydrogenation and C–C coupling, while hardly affecting the HER. Therefore, Cu with tensile strain is expected to exhibit higher overall CO_2RR selectivity and suppressed HER, compared to unstrained Cu. Figure 5b displays the product distributions on the three catalysts at $-1.1 \text{ V}_{\text{RHE}}$, in which the differences in the production of H_2 , CH_4 , and C_1 compounds between strained (Cu(OH)₂- and Cu₂(OH)₂CO₃-derived) and unstrained (CuO-derived) Cu are clearly illustrated. In comparison with the unstrained Cu, the strained Cu exhibited higher $\text{FE}_{\text{CO}_2\text{RR}}$, primarily contributed by the enhanced production of C_1 compounds (e.g., CH_4), and lower FE_{H_2} . This result is consistent with expectations from DFT calculations, corroborating the important role that lattice strain in Cu may play in CO_2RR .

It is not fully understood why Cu nanocrystals derived from Cu(OH)₂ or Cu₂(OH)₂CO₃ have greater tensile strain than Cu nanocrystals derived from CuO. One possible reason is that the former nanocrystals undergo more drastic shrinkage in unit-cell volume (74% for Cu₂(OH)₂CO₃, 71% for Cu(OH)₂, and 42% for CuO; Supplementary Table 3) and more pronounced elimination of components than the latter nanocrystals during the phase transition. With this hypothesis, the degree of lattice strain in Cu crystals can be tuned by the precursors, offering an effective strategy for strain engineering.

Although the promoting effect of tensile strain on C–C coupling and suppression on the competing HER have been demonstrated theoretically^{60,61}, a controversy exists in the literature on how the tensile strain in Cu affects the C_1 products during the CO_2RR . For instance, a recent study reported that tensile strain in Cu is unfavorable for the formation of C_1 products²⁹, which is inconsistent with our observations and the conclusions of other studies^{31,61}. Another study

concluded that tensile strain has different effects on the production of CH₄, depending on the thickness of the Cu layer³⁰. These discrepancies imply that the lattice strain is not the primary factor determining CO₂RR selectivity, and its effect may be overwhelmed by other coexisting factors, such as crystal size, grain boundary, and alloying effect. In this study, the high C₂₊ selectivity of derived Cu catalysts is primarily attributed to the grain boundaries and high-index facets due to the size effect, while the overall CO₂RR selectivity (influenced by the competition between C₁ production and HER) can be further improved by introducing tensile strain through the choice of precursors.

In summary, the as-prepared Cu₂(OH)₂CO₃, Cu(OH)₂, and CuO nanocrystals delivered an FE_{C₂₊} of 73.0%, 71.9%, and 68.6%, respectively, at approximately -1.1 V_{RHE} during the CO₂RR. The time-resolved *operando* XRD, which uses a laboratory-scale X-ray source for characterizing CO₂RR electrocatalysts, and *operando* Raman spectroscopy confirmed the full reduction of the precursors to Cu(O) while (or before) delivering enhanced C₂₊ selectivity under CO₂RR conditions, and revealed that the electroreduction kinetics of Cu₂(OH)₂CO₃ and Cu(OH)₂ were significantly slower than those of CuO. The results collectively demonstrated that the active species responsible for the enhanced C₂₊ selectivity of the derived Cu electrodes was Cu(O), rather than oxidized Cu species. This conclusion was further verified by the faster reduction of CuO to Cu and the corresponding higher FE_{C₂H₄} at the initial stage of CO₂RR compared to that of Cu₂(OH)₂CO₃. However, it is worth noting that the possible presence of dynamic amorphous oxidized Cu species in the catalyst cannot be completely excluded due to the inherent limitations of XRD and Raman characterization.

A negative correlation between the Cu grain size and C₂₊ selectivity was established and the small grain size of the derived Cu (-11 nm), which resulted in an increased exposure of grain boundaries and high-index facets to facilitate the C-C coupling reaction, was considered as the primary factor for achieving high C₂₊ selectivity. *Operando* XRD revealed remarkable tensile strains in Cu nanocrystals derived from Cu(OH)₂ and Cu₂(OH)₂CO₃ but not in Cu nanocrystals derived from CuO. Theoretical calculations indicate that tensile strain in the Cu lattice helps promote the hydrogenation of *CO and C-C coupling, enhancing the overall CO₂RR selectivity and suppressing HER, which explains the diverse performance of the three derived Cu catalysts. Reducing crystallite size and inducing lattice strain were therefore identified as two effective approaches to enhancing the performance of Cu catalysts for CO₂RR.

The findings of this study highlight the significant role of *operando* characterization techniques in probing catalyst evolution during CO₂RR, and the customized *operando* platforms can be readily adapted to other important electrochemical reactions, including but not limited to hydrogen/oxygen evolution, nitrogen reduction, and methane oxidation.

Methods

Precursor preparation

Cu₂(OH)₂CO₃ nanocrystals and CuO nanocrystals. First, aqueous solutions of 10 mL of 0.5 M CuSO₄ (Sigma-Aldrich, 98%) and 12 mL of 0.5 M Na₂CO₃ (Sigma-Aldrich, ≥99.0%) were prepared at room temperature using Milli-Q water (18.2 MΩ·cm⁻¹). Subsequently, the Na⁺ solution was added to the Cu²⁺ solution, and the mixture was continuously stirred. After 15 min, the mixture was heated at 60 °C and stirred for another 15 min. Afterward, the mixture was allowed to stand until fully precipitated. Then, the Cu₂(OH)₂CO₃ nanocrystals were obtained via vacuum filtration. The final product was dried in a vacuum oven overnight at 30 °C. The as-prepared Cu₂(OH)₂CO₃ nanocrystals were heated in a vacuum oven for 4 days at 250 °C to synthesize CuO nanocrystals.

Cu(OH)₂ nanocrystals. First, 50 mL of 0.05 M aqueous solution of Cu(NO₃)₂ was prepared at room temperature. Subsequently, 1 mL of

25% ammonia solution was slowly added into the solution, followed by 1 mL of 0.01 M NaOH aqueous solution under stirring. The mixture was heated to 60 °C for 15 min and then cooled to room temperature. Then, the mixture was subjected to centrifugation and copious washing with water to a neutral pH to obtain the resulting bluish Cu(OH)₂ nanocrystals. The final product was dried in a vacuum oven overnight at 30 °C.

Cu nanowires and electropolished Cu foil. The Cu nanowires were sequentially prepared by mixing 20 mL of 15 M NaOH, 1 mL of 0.1 M Cu(NO₃)₂, 0.15 mL of ethylenediamine, and 0.025 mL of 35 wt% hydrazine under continuous stirring. Subsequently, the mixture was heated to 80 °C for 60 min, and the product was collected by centrifugation and washed with a 3 wt% aqueous hydrazine solution. The Cu nanowires were dried in a vacuum oven overnight at 30 °C and stored under an Ar atmosphere to minimize oxidation. Polycrystalline Cu foil was electropolished in 85% phosphoric acid (Scharlau, 85% in water) at 3.0 V vs. another Cu foil for 5 min.

Ex situ material characterization

The chemical compositions of the precursors were investigated using powder XRD (Bruker, D8 Advance) with a Cu Kα radiation wavelength of 0.154184 nm. The obtained peaks were indexed using standard patterns (PDF#00-004-0836 for Cu, PDF#00-048-1548 for CuO, PDF#04-009-4366 for Cu(OH)₂, and PDF#00-002-0345 for Cu₂(OH)₂CO₃). The mean crystallite sizes of the precursors were estimated using the Scherrer equation ($\tau = K\lambda/\beta\cos\theta$, where τ is the mean size of the crystalline domains, K is the dimensionless shape factor (0.89), λ is the X-ray wavelength, β is the line broadening at half the maximum intensity (full width at half maximum), and θ is the Bragg angle). Ex situ Raman spectra of the samples were recorded using a WITec apyron system equipped with a 633 nm laser. Considering that the three compounds were easily reduced to Cu₂O under the Raman laser (Supplementary Fig. 19)³⁶, a low magnification objective lens (Zeiss EC Epiplan-Neofluar Dic 10X/0.25) was used and the laser power was set to 20 mW to prevent the laser-induced thermo-reduction of the samples. The surface morphologies of the samples were characterized using SEM (FEI, Magellan) at a working distance of 4 mm. All samples were coated with a layer of 3 nm of Ir prior to SEM imaging to eliminate charging caused by their poor conductivity.

Electrode preparation

First, 20 mg of the as-prepared precursor powder was mixed with 50 μL of Nafion solution and 3 mL of ethanol. Subsequently, the mixture was sonicated for at least 30 min to obtain a homogenous ink. Next, the electrodes were prepared by airbrushing the precursor ink onto a glassy carbon substrate with an area of 1.0 × 0.5 cm². For *operando* characterizations, carbon paper (Freudenberg H14C9, Fuel Cell Store) was used as the substrate. The mass loading of the precursor was approximately 0.6 mg cm⁻².

Electroreduction of CO₂

The electrochemistry experiments were performed in a gas-tight H-type cell using a CHI 760e workstation. The cathode and anode compartments were separated using a Nafion 117 membrane (Fuel Cell Store). A Pt foil was used as the counter electrode, and an Ag/AgCl electrode filled with saturated KCl solution (CHI, 111) was used as the reference electrode. All potentials measured against Ag/AgCl were converted to the reversible hydrogen electrode (RHE) scale using $E_{\text{RHE}} = E_{\text{Ag/AgCl}} + 0.197 \text{ V} + 0.0591 \times \text{pH}$. The cell resistance was determined using a current-interrupt method, and the potential was manually corrected after each measurement. In addition, a 0.1 M KHCO₃ (Honeywell, 99.5% to 101.0% (acidimetric)) aqueous solution was used as the electrolyte and was saturated with CO₂ prior to each CO₂RR experiment. The pH value of the cell measured using an Orion 5 star

benchtop multiparameter (Thermo Scientific) was 6.8. During the CO₂RR experiment, 5.0 sccm of CO₂ was continuously purged into the cell, and the gaseous products were routed into an online gas chromatography (GC) system (Kechuang GC2002).

Product analysis

Gaseous products were detected using the online GC equipped with three detectors: one thermal conductivity detector for detecting H₂, one flame ionization detector for detecting hydrocarbons, and another flame ionization detector coupled with a methanizer (Kechuang) for detecting CO. Quantitative determination was conducted using calibration curves from standard gases.

Liquid products were analyzed using proton nuclear magnetic resonance (NMR, Bruker, 600 MHz) with a presaturation sequence for suppressing the water peak. Calibration curves were developed using commercial chemicals with 1.67 ppm dimethyl sulfoxide (Sigma-Aldrich, 99.9%) as the internal standard. In addition, FE was calculated using $FE = ([A] \cdot V \cdot (nF))/Q$, where $[A]$ is the analyte concentration determined using quantitative NMR, V represents the NMR sample volume (typically, 600 μ L), n denotes the molar ratio of the transferred electrons, F indicates the Faraday constant, and Q denotes the total charge passed.

Operando XRD

Operando XRD measurements were performed using a Bruker D8 Discover XRD spectrometer equipped with an I μ S microfocus X-ray source and Eiger 2D detector. A 2 mm collimator was used to enhance the X-ray intensity on a small spot on the electrode. The 2D detector was vertically positioned to enable the coverage of 21.7° (2 θ) in the still scan mode to cover the desired diffraction angle range at a high resolution (Supplementary Fig. 20). In addition, an optical laser-video camera system was incorporated to enable easy and accurate sample positioning and system alignment. A customized electrochemical cell (Supplementary Fig. 6) was used with a Pt wire and an Ag/AgCl electrode (CHI 111; saturated KCl solution) as the counter and reference electrodes, respectively. The cathode and anode compartments were separated using a Fumasep FKB-PK-130 membrane (Fuel Cell Store). The precursors were airbrushed onto one side of the carbon paper and positioned close to the glassy carbon on the cell to function as the working electrode. The electrolyte (50 mL of 0.1 M KHCO₃) was saturated with CO₂ while circulating through the cell at 1 mL min⁻¹. During the measurements, the cell was fastened on the stage using psi tilted to 30° for the better release of in situ formed bubbles from the electrode surface. For the Cu₂(OH)₂CO₃ nanocrystals, the measurements were conducted at -0.84, -1.05, and -1.2 V_{RHE}. For Cu(OH)₂ and CuO nanocrystals, the potential was set to -1.08 and -1.16 V_{RHE}, respectively. The 2D diffraction patterns were collected in the still scan mode at an integration time of 900 s. The raw data were integrated using DIFFRAC.EVA software, and the background was removed for improved peak identification.

Strain determination

The tensile strain values of derived Cu samples were calculated using the equation:

$$\text{Tensile strain (\%)} = \frac{d - d_0}{d_0} \times 100\% \quad (1)$$

where d is the d -spacing of a given reflection (e.g., Cu(111) or Cu(100)) determined from the XRD pattern and d_0 is the corresponding d -spacing in the standard Cu sample.

For the operando XRD experiments, the theta angle was set to 20.28° for still scan mode to achieve the desired diffraction angle range (30°–51.7°, 2 θ) at a high resolution. Under such conditions, the

illuminated area on the electrode is an ellipse of ~4.7 mm². The obtained strain value is the average result of the illuminated area.

Operando Raman spectroscopy

Operando Raman spectra were recorded using a WITec apyron system with a water-immersion objective lens (Zeiss W Plan-Apochromat 63X/1) and a 633 nm laser beam. A low laser power of 0.8 mW was used to prevent the irradiation-induced modification on the precursor surface. The measurements were conducted in a customized electrochemical cell (Supplementary Fig. 10) with a Pt wire and an Ag/AgCl electrode (CHI 111; saturated KCl solution) as the counter and reference electrode, respectively. The cathode and anode compartments were separated using a Fumasep FKB-PK-130 membrane (Fuel Cell Store). The electrolyte (50 mL of 0.1 M KHCO₃) was saturated with CO₂ while circulating at 1 mL min⁻¹ above the electrode surface to remove bubbles produced in situ. The Raman signals were collected in a back-scattering geometry every 15 min along the CO₂RR process. The raw data were recorded and processed using WITec Control Five software, and the background was removed to enable improved peak identification.

Computational methods

The DFT calculations were conducted using the projector-augmented wave method, as implemented in Vienna Ab initio Simulation Package code^{62,63}. The generalized gradient approximation with the Perdew–Burke–Ernzerhof exchange-correlation functional was used. A uniform 6 \times 6 \times 6 k -mesh grid in the Brillouin zone was employed to optimize the crystal structure of bulk Cu, and the resulting lattice parameter was $a = 3.635$ Å. The Cu slab model with five atomic layers had a (2 \times 2) and a (3 \times 3) lateral periodicity with (111) and (100) exposed surfaces, respectively, and the slab replica was separated by ~20 Å of vacuum. The lattice parameters were set to $a = 3.653$ Å, 3.671 Å, 3.690 Å, and 3.708 Å for Cu(111) and Cu(100) slabs to mimic 0.5%, 1.0%, 1.5%, and 2.0% tensile strain, respectively. A 2 \times 2 \times 1 k -mesh was used for all Cu(111) and Cu(100) slab structures. The plane-wave basis set cutoffs of the wave functions were set at 500 eV for the bulk and 450 eV for slab structures without and with molecular adsorption. The atomic positions of all structures were fully relaxed until the forces on each atom were less than 0.01 eV/Å.

The Gibbs free energy values were calculated using the following equations:

$$G = E_{\text{DFT}} + E_{\text{ZPE}} + \int_0^{298.15} C_v dT - TS \quad (2)$$

$$E_{\text{ZPE}} = \frac{1}{2} \sum h\nu \quad (3)$$

$$\int_0^{298.15} C_v dT = k_B \sum \left(\frac{h\nu}{k_B T} \right)^2 \frac{\exp\left(\frac{h\nu}{k_B T}\right)}{\left[\exp\left(\frac{h\nu}{k_B T}\right) - 1 \right]^2} \quad (4)$$

where E_{DFT} denotes the energy calculated by DFT, E_{ZPE} represents the vibrational zero-point energy, $\int_0^{298.15} C_v dT$ indicates the heat capacity, and S is the entropy, respectively. In addition, h is the Planck constant, k_B denotes the Boltzmann constant, and ν represents the vibrational frequency. Only vibrational modes were considered for calculating the entropy due to the scarce contribution from translational and rotational modes. The Gibbs free energy of formation ($\Delta G_{\text{formation}}$) for *COCO is calculated as $\Delta G_{\text{formation}}(*\text{COCO}) = G_{*\text{COCO}} - (G_{*\text{CO}} + G_{\text{H}_2/2})$. In addition, $\Delta G_{\text{formation}}$ for *COH is calculated as $\Delta G_{\text{formation}}(*\text{COH}) = G_{*\text{COH}} - (G_{*\text{CO}} + G_{\text{H}_2/2})$, $\Delta G_{\text{formation}}$ for *CHO is calculated as $\Delta G_{\text{formation}}(*\text{CHO}) = G_{*\text{CHO}} - (G_{*\text{CO}} + G_{\text{H}_2/2})$, and $\Delta G_{\text{formation}}$ for *COCO is calculated as $\Delta G_{\text{formation}}(*\text{COCO}) = G_{*\text{COCO}} - (G_{*\text{CO}} + G_{\text{CO}})$. The

thermodynamic parameters for calculating Gibbs free energies are given in Supplementary Tables S4–S13.

The hydrogen adsorption free energy G_{H} is calculated as $G_{\text{H}} = E(\text{slab} + \text{H}) - E(\text{slab}) - E(\text{H}_2)/2 + \Delta E_{\text{ZPE}} - T\Delta S$, where $E(\text{slab} + \text{H})$ and $E(\text{slab})$ are the total energies of the Cu(111) or Cu(100) slab with and without H adsorption; $E(\text{H}_2)$ is the total energy of a H_2 molecule; ΔE_{ZPE} is the difference in the zero-point energy between gas phase of H_2 and the adsorbed H atom; and ΔS is the difference in entropy. To determine the transition state (TS) for the water dissociation on the Cu(111) and Cu(100) surfaces, the climbing image nudged elastic band (NEB) method was employed, and the force convergence tolerance on each atom was set to be 0.05 eV/Å during the search of the minimum energy path.

Data availability

The data supporting the findings of this study are provided in the Supplementary Information/Source Data file. The input and output files for the DFT calculations are available in the IoChem-BD database (<https://iochem-bd.bsc.es/browse/review-collection/100/215881/6ca411524a36a3f2c1194679>). Additional data are available from the corresponding authors on request. Source data are provided with this paper.

Code availability

Vienna ab initio simulation package (VASP) for the DFT calculations is available at <https://www.vasp.at/>.

References

- Gao, D. F., Arán-Ais, R. M., Jeon, H. S. & Roldan Cuenya, B. Rational catalyst and electrolyte design for CO_2 electroreduction towards multicarbon products. *Nat. Catal.* **2**, 198–210 (2019).
- Xia, C. et al. Continuous production of pure liquid fuel solutions via electrocatalytic CO_2 reduction using solid-electrolyte devices. *Nat. Energy* **4**, 776–785 (2019).
- Zheng, T. T. et al. Large-scale and highly selective CO_2 electrocatalytic reduction on nickel single-atom catalyst. *Joule* **3**, 265–278 (2019).
- Lu, L. et al. Highly efficient electroreduction of CO_2 to methanol on palladium-copper bimetallic aerogels. *Angew. Chem. Int. Ed. Engl.* **57**, 14149–14153 (2018).
- Wang, Y. S., Chen, J. X., Wang, G. X., Li, Y. & Wen, Z. H. Per-fluorinated covalent triazine framework derived hybrids for the highly selective electroconversion of carbon dioxide into methane. *Angew. Chem. Int. Ed.* **57**, 13120–13124 (2018).
- Fan, L. et al. Strategies in catalysts and electrolyzer design for electrochemical CO_2 reduction toward C_{2+} products. *Sci. Adv.* **6**, eaay3111 (2020).
- Lei, Q. et al. Investigating the Origin of Enhanced C_{2+} Selectivity in Oxide-/Hydroxide-Derived Copper Electrodes during CO_2 Electroreduction. *J. Am. Chem. Soc.* **142**, 4213–4222 (2020).
- Lee, S. Y. et al. Mixed copper states in anodized Cu electrocatalyst for stable and selective ethylene production from CO_2 reduction. *J. Am. Chem. Soc.* **140**, 8681–8689 (2018).
- Liang, Z. Q. et al. Copper-on-nitride enhances the stable electro-synthesis of multi-carbon products from CO_2 . *Nat. Commun.* **9**, 3828 (2018).
- Van Muylder, J. *Electrochemical Materials Science* Ch. 1 (Springer US: Boston, MA, 1981).
- Mistry, H. et al. Highly selective plasma-activated copper catalysts for carbon dioxide reduction to ethylene. *Nat. Commun.* **7**, 12123 (2016).
- Fan, Q. K. et al. Manipulating Cu nanoparticle surface oxidation states tunes catalytic selectivity toward CH_4 or C_{2+} products in CO_2 electroreduction. *Adv. Energy Mater.* **11**, 2101424 (2021).
- Yang, P. P. et al. Protecting copper oxidation state via intermediate confinement for selective CO_2 electroreduction to C_{2+} . *Fuels. J. Am. Chem. Soc.* **142**, 6400–6408 (2020).
- Liu, C. et al. Stability and effects of subsurface oxygen in oxide-derived Cu catalyst for CO_2 reduction. *J. Phys. Chem. C.* **121**, 25010–25017 (2017).
- Favaro, M. et al. Subsurface oxide plays a critical role in CO_2 activation by Cu(111) surfaces to form chemisorbed CO_2 , the first step in reduction of CO_2 . *Proc. Natl Acad. Sci. USA* **114**, 6706–6711 (2017).
- Dattila, F., García-Muelas, R. & López, N. Active and selective ensembles in oxide-derived copper catalysts for CO_2 reduction. *ACS Energy Lett.* **5**, 3176–3184 (2020).
- Eilert, A. et al. Subsurface oxygen in oxide-derived copper electrocatalysts for carbon dioxide reduction. *J. Phys. Chem. Lett.* **8**, 285–290 (2017).
- Cavalca, F. et al. Nature and distribution of stable subsurface oxygen in copper electrodes during electrochemical CO_2 reduction. *J. Phys. Chem. C.* **121**, 25003–25009 (2017).
- Wang, H. Y. et al. Direct evidence of subsurface oxygen formation in oxide-derived Cu by X-ray photoelectron spectroscopy. *Angew. Chem. Int. Ed.* **61**, e20211021 (2022).
- Scholten, F., Nguyen, K. C., Bruce, J. P., Heyde, M. & Roldan Cuenya, B. Identifying structure-selectivity correlations in the electrochemical reduction of CO_2 : A comparison of well-ordered atomically clean and chemically etched copper single-crystal surfaces. *Angew. Chem. Int. Ed. Engl.* **60**, 19169–19175 (2021).
- Kim, T. et al. Enhancing $\text{C}_2\text{--C}_3$ production from CO_2 on copper electrocatalysts via a potential-dependent mesostructure. *ACS Appl. Energy Mater.* **1**, 1965–1972 (2018).
- Jiang, K. et al. Metal ion cycling of Cu foil for selective C-C coupling in electrochemical CO_2 reduction. *Nat. Catal.* **1**, 111–119 (2018).
- Möller, T. et al. Electrocatalytic CO_2 reduction on CuO_x Nanocubes: Tracking the evolution of chemical state, geometric structure, and catalytic selectivity using Operando spectroscopy. *Angew. Chem. Int. Ed. Engl.* **59**, 17974–17983 (2020).
- Velasco-Velez, J. J. et al. Revealing the active phase of copper during the electroreduction of CO_2 in aqueous electrolyte by correlating in situ X-ray spectroscopy and in situ electron microscopy. *ACS Energy Lett.* **5**, 2106–2111 (2020).
- Jansonius, R. P., Reid, L. M., Virca, C. N. & Berlinguette, C. P. Strain engineering electrocatalysts for selective CO_2 reduction. *ACS Energy Lett.* **4**, 980–986 (2019).
- Mavrikakis, M., Hammer, B. & Nørskov, J. K. Effect of strain on the reactivity of metal surfaces. *Phys. Rev. Lett.* **81**, 2819–2822 (1998).
- Liu, F. Z., Wu, C. & Yang, S. C. Strain and Ligand Effects on CO_2 Reduction Reactions over Cu-Metal Heterostructure Catalysts. *J. Phys. Chem. C.* **121**, 22139–22146 (2017).
- Monzó, J. et al. Enhanced electrocatalytic activity of Au@Cu core@shell nanoparticles towards CO_2 reduction. *J. Mater. Chem. A* **3**, 23690–23698 (2015).
- Kim, T., Kumar, R. E., Brock, J. A., Fullerton, E. E. & Fenning, D. P. How Strain Alters CO_2 Electroreduction on Model Cu(001) Surfaces. *ACS Catal.* **11**, 6662–6671 (2021).
- Du, M. S., Zhao, X., Zhu, G., Hsu, H. Y. & Liu, F. Elastic strain controlling the activity and selectivity of CO_2 electroreduction on Cu overlayers. *J. Mater. Chem. A* **9**, 4933–4944 (2021).
- Liu, S. G. & Huang, S. P. Structure engineering of Cu-based nanoparticles for electrochemical reduction of CO_2 . *J. Catal.* **375**, 234–241 (2019).
- Li, C. W., Ciston, J. & Kanan, M. W. Electroreduction of carbon monoxide to liquid fuel on oxide-derived nanocrystalline copper. *Nature* **508**, 504–507 (2014).

33. Chen, C. J. et al. The in situ study of surface species and structures of oxide-derived copper catalysts for electrochemical CO₂ reduction dagger. *Chem. Sci.* **12**, 5938–5943 (2021).
34. Li, X., Wang, S., Li, L., Sun, Y. & Xie, Y. Progress and perspective for in situ studies of CO₂ reduction. *J. Am. Chem. Soc.* **142**, 9567–9581 (2020).
35. Jiang, S., Klingan, K., Pasquini, C. & Dau, H. New aspects of operando Raman spectroscopy applied to electrochemical CO₂ reduction on Cu foams. *J. Chem. Phys.* **150**, 041718 (2019).
36. Deng, Y. L., Handoko, A. D., Du, Y. H., Xi, S. B. & Yeo, B. S. In situ Raman spectroscopy of copper and copper oxide surfaces during electrochemical oxygen evolution reaction: Identification of Cu^{III} oxides as catalytically active species. *ACS Catal.* **6**, 2473–2481 (2016).
37. Marucci, G., Beeby, A., Parker, A. W. & Nicholson, C. E. Raman spectroscopic library of medieval pigments collected with five different wavelengths for investigation of illuminated manuscripts. *Anal. Methods-UK* **10**, 1219–1236 (2018).
38. Frost, R. L., Martens, W. N., Rintoul, L., Mahmutagic, E. & Klopogge, J. T. Raman spectroscopic study of azurite and malachite at 298 and 77 K. *J. Raman Spectrosc.* **33**, 252–259 (2002).
39. Wang, W. et al. A simple wet-chemical synthesis and characterization of CuO nanorods. *Appl. Phys. A* **76**, 417–420 (2003).
40. Cheng, D. et al. The nature of active sites for carbon dioxide electroreduction over oxide-derived copper catalysts. *Nat. Commun.* **12**, 395 (2021).
41. Dutta, A. et al. CO₂ electrolysis - Complementary operando XRD, XAS and Raman spectroscopy study on the stability of Cu_xO foam catalysts. *J. Catal.* **389**, 592–603 (2020).
42. Ren, D., Gao, J., Zakeeruddin, S. M. & Grätzel, M. New insights into the interface of electrochemical flow cells for carbon dioxide reduction to ethylene. *J. Phys. Chem. Lett.* **12**, 7583–7589 (2021).
43. Moradzaman, M. & Mul, G. In situ Raman study of potential-dependent surface adsorbed carbonate, CO, OH, and C species on Cu electrodes during electrochemical reduction of CO₂. *Chem-electrochemistry* **8**, 1478–1485 (2021).
44. Shan, W. et al. In situ surface-enhanced Raman spectroscopic evidence on the origin of selectivity in CO₂ electrocatalytic reduction. *ACS Nano* **14**, 11363–11372 (2020).
45. Schmitt, K. G. & Gewirth, A. A. In situ surface-enhanced Raman spectroscopy of the electrochemical reduction of carbon dioxide on silver with 3,5-Diamino-1,2,4-Triazole. *J. Phys. Chem. C* **118**, 17567–17576 (2014).
46. Liu, G. et al. CO₂ reduction on pure Cu produces only H₂ after subsurface O is depleted: Theory and experiment. *Proc. Natl Acad. Sci. USA* **118**, e2012649118 (2021).
47. Scott, S. B. et al. Absence of Oxidized Phases in Cu under CO Reduction Conditions. *ACS Energy Lett.* **4**, 803–804 (2019).
48. Feng, X., Jiang, K., Fan, S. & Kanan, M. W. A direct grain-boundary-activity correlation for CO electroreduction on Cu nanoparticles. *ACS Cent. Sci.* **2**, 169–174 (2016).
49. Handoko, A. D. et al. Mechanistic Insights into the selective electroreduction of carbon dioxide to ethylene on Cu₂O-derived copper catalysts. *J. Phys. Chem. C* **120**, 20058–20067 (2016).
50. Jung, H. et al. Electrochemical fragmentation of Cu₂O nanoparticles enhancing selective C-C coupling from CO₂ reduction reaction. *J. Am. Chem. Soc.* **141**, 4624–4633 (2019).
51. Velasco-Vélez, J. J. et al. On the activity/selectivity and phase stability of thermally grown copper oxides during the electrocatalytic reduction of CO₂. *ACS Catal.* **10**, 11510–11518 (2020).
52. Lum, Y. W., Yue, B. B., Lobaccaro, P., Bell, A. T. & Ager, J. W. Optimizing C-C Coupling on Oxide-Derived Copper Catalysts for Electrochemical CO₂ Reduction. *J. Phys. Chem. C* **121**, 14191–14203 (2017).
53. Chen, Z. Q. et al. Grain-Boundary-rich copper for efficient solar-driven electrochemical CO₂ reduction to ethylene and ethanol. *J. Am. Chem. Soc.* **142**, 6878–6883 (2020).
54. Nitopi, S. et al. Progress and Perspectives of Electrochemical CO₂ Reduction on Copper in Aqueous Electrolyte. *Chem. Rev.* **119**, 7610–7672 (2019).
55. Zhan, C. et al. Revealing the CO Coverage-Driven C-C Coupling Mechanism for Electrochemical CO₂ Reduction on Cu₂O Nanocubes via Operando Raman Spectroscopy. *ACS Catal.* **11**, 7694–7701 (2021).
56. Zheng, Y. et al. Understanding the Roadmap for Electrochemical Reduction of CO₂ to Multi-Carbon Oxygenates and Hydrocarbons on Copper-Based Catalysts. *J. Am. Chem. Soc.* **141**, 7646–7659 (2019).
57. De Luna, P. et al. Catalyst electro-redeposition controls morphology and oxidation state for selective carbon dioxide reduction. *Nat. Catal.* **1**, 103–110 (2018).
58. Kortlever, R., Shen, J., Schouten, K. J. P., Calle-Vallejo, F. & Koper, M. T. M. Catalysts and Reaction Pathways for the Electrochemical Reduction of Carbon Dioxide. *J. Phys. Chem. Lett.* **6**, 4073–4082 (2015).
59. Birdja, Y. Y. et al. Advances and challenges in understanding the electrocatalytic conversion of carbon dioxide to fuels. *Nat. Energy* **4**, 732–745 (2019).
60. Sandberg, R. B., Montoya, J. H., Chan, K. & Nørskov, J. K. CO-CO coupling on Cu facets: Coverage, strain and field effects. *Surf. Sci.* **654**, 56–62 (2016).
61. Chen, Z. Z., Zhang, X. & Lu, G. Overpotential for CO₂ electroreduction lowered on strained penta-twinned Cu nanowires. *Chem. Sci.* **6**, 6829–6835 (2015).
62. Kresse, G. & Hafner, J. Ab-Initio Molecular-Dynamics for Open-Shell Transition-Metals. *Phys. Rev. B* **48**, 13115–13118 (1993).
63. Kresse, G. & Furthmüller, J. Efficient iterative schemes for ab initio total-energy calculations using a plane-wave basis set. *Phys. Rev. B* **54**, 11169–11186 (1996).

Acknowledgements

The financial support for this work was provided by KAUST Catalysis Center CCF Fund (FCC/1/1974-16-01) to Y.H. and Baseline Funds (BAS/1/1413-01-01) to X.L. from King Abdullah University of Science and Technology. This work is partially supported by National Key Research and Development Project of China (2022YFE0113800). This research used resources from the Core Laboratories of King Abdullah University of Science and Technology. J.Y. acknowledges financial support from the Hong Kong Polytechnic University (grant P0042930).

Author contributions

Q.L. and Y.H. crafted the experimental plan and analyzed all the data. Q.L. performed the precursor synthesis, CO₂RR performance evaluation, and the operando XRD. Q.L., L.H., K.X.Y., X.W., Z.W., and Y.H. analyzed the CO₂RR results. Q.L., B.D., and Y.Y. designed and implemented the operando XRD characterization platform. Q.L. and L.H. implemented and performed the operando Raman spectroscopy characterization under the guidance of X.L. J.Y. performed the theoretical calculations and analyzed the computational data. X.D. implemented the online gas chromatography system. Y.H. guided the research. Q.L., Y.H., and X.L. wrote the manuscript. All the authors discussed the results and reviewed the manuscript.

Competing interests

The authors declare no competing interests.

Additional information

Supplementary information The online version contains supplementary material available at <https://doi.org/10.1038/s41467-022-32601-9>.

Correspondence and requests for materials should be addressed to Jun Yin, Xu Lu or Yu Han.

Peer review information *Nature Communications* thanks the other anonymous reviewer(s) for their contribution to the peer review of this work.

Reprints and permission information is available at <http://www.nature.com/reprints>

Publisher's note Springer Nature remains neutral with regard to jurisdictional claims in published maps and institutional affiliations.

Open Access This article is licensed under a Creative Commons Attribution 4.0 International License, which permits use, sharing, adaptation, distribution and reproduction in any medium or format, as long as you give appropriate credit to the original author(s) and the source, provide a link to the Creative Commons license, and indicate if changes were made. The images or other third party material in this article are included in the article's Creative Commons license, unless indicated otherwise in a credit line to the material. If material is not included in the article's Creative Commons license and your intended use is not permitted by statutory regulation or exceeds the permitted use, you will need to obtain permission directly from the copyright holder. To view a copy of this license, visit <http://creativecommons.org/licenses/by/4.0/>.

© The Author(s) 2022